ACS OMEGA

http://pubs.acs.org/journal/acsodf

Article

Open Access

This article is licensed under CC-BY 4.0

Downloaded via UNIV OF SAO PAULO on May 27, 2025 at 10:45:59 (UTC).
See https://pubs.acs.org/sharingguidelines for options on how to legitimately share published articles.

Influence of Ion Substitution on the Properties of Apatite-Based Materials: Computational Predictions Using Density Functional Theory

Henrique S. Marques, Albert F. B. Bittencourt, and Juarez L. F. Da Silva*

Cite This: https://doi.org/10.1021/acsomega.4c09997

Read Online

ACCESS | Metrics & More | Article Recommendations | Supporting Information

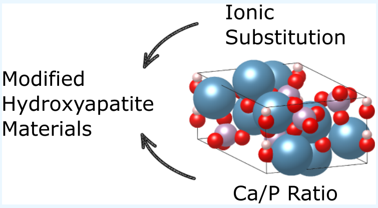

ABSTRACT: Apatite-based materials have attracted recognition as promising candidates for catalytic applications because of their tunable properties that can be achieved through ionic substitutions and their compatibility with sustainability goals for environmentally friendly catalysts. However, a thorough understanding of their physicochemical properties at the atomic level remains insufficient. In this study, calculations based on density functional theory combined with Spearman's correlation are used to investigate the effects of cationic and anionic substitutions on the structural, energetic, and electronic properties of materials similar to apatite with Ca/P ratios ranging from 0.50 to 2.00. Our results reveal that substitutions with d-block elements, such as Zn and Cd, reduce the energy gap at the Γ-point and decrease the ionic character of the materials, leading to reduced stability. Additionally, d-p orbital hybridization within the PO_4^{3-}, AsO_4^{3-}, and VO_4^{3-} groups significantly influences structural stability. Using Spearman's correlation analysis, we identified significant trends, specifically indicating a strong correlation between net atomic charges, energy gaps, and cohesive energy. These results offer critical insights into how ionic substitutions influence the tunable characteristics of materials resembling apatite.

1. INTRODUCTION

Apatite-based materials, which comprise a class of compounds based on hydroxyapatite (HAP), have been identified as promising candidates within the domain of heterogeneous catalysis. HAP has a specific chemical formula $C_{10}(PO_4)_6(OH)_2$, which contains cationic (Ca^{2+}) and anionic (PO_4^{3-}, OH^{1-}) species within the crystal structure. Thus, it leads to the presence of both acidic and basic active sites on the surface of HAP particles, which helps to explain its success in catalysis.[1−3] This unique set of features also opens the possibility for its utilization in a broad range of catalytic processes, including carbon−carbon cross-coupling,[4] condensation,[5] oxidation reactions,[6] and more.[7] Furthermore, HAP is consistent with the principles of green chemistry[8] owing to its nontoxicity, high stability, reusability, and abundance.[9] These attributes establish HAP as an alternative to traditional catalysts, especially in the context of sustainable chemistry applications.[10]

An outstanding characteristic of HAP is its remarkable ion-exchange capacity,[11] allowing the substitution of calcium ions (Ca^{2+}) and phosphate groups (PO_4^{3-}) with various cations (e.g., Mg^{2+},[12] Sr^{2+},[13] Ba^{2+},[14] Fe^{2+},[14] Zn^{2+}[15]) and anions (e.g., CO_2^{3-},[16] AsO_4^{3-},[17] VO_4^{3-}[18]), respectively. Thus, the ion exchange capability allows for fine-tuning of surface reactivity, optimizing acidic, basic, and redox properties for targeted catalytic applications.[19] For example, Ho et al.[20] demonstrated that the activity of HAP catalysts can be modulated by substituting Ca^{2+} with other alkaline earth metals, which affects the strength of the acidic and basic sites, enhancing the stabilization of intermediate species during condensation reactions. Similarly, Ramesh et al.[21] showed that replacing PO_4^{3-} with anions such as WO_4^{2-} or SO_4^{2-} can regulate dehydrogenation and dehydration activities in ethanol conversion processes.

As recognized by Yook et al.,[19] the adaptability of HAP as a catalytic material can be significantly increased through the concurrent substitution of multiple elements. Given that various interchangeable sites are available in the HAP structure (i.e., Ca^{2+}, PO_4^{3-}, and OH^-), multiple substitutions could maximize catalytic efficiency and expand the potential applications of HAP-based catalysts. Although only a few studies have explored this direction, it has been shown that substitutions with elements such as Ni and Ce in HAP have the potential to enhance catalytic performance.[22] In recent studies, Gadipelly et al.[23] investigated the efficacy of doping HAP in facilitating bond formation reactions, specifically focusing on the C−C and C−N bonds.

In its stoichiometric composition, HAP is characterized by a Ca/P molar ratio of 1.67. However, this ratio is subject to variation based on the synthesis techniques applied, which leads to diverse crystallographic structures exhibiting distinct morphologies and distributions of surface sites.[19] For instance, varying the Ca/P ratio permits the acquisition of different phases, such as monocalcium phosphate anhydrous (Ca-

Received: November 2, 2024
Revised: May 16, 2025
Accepted: May 19, 2025

ACS Publications

© XXXX The Authors. Published by American Chemical Society

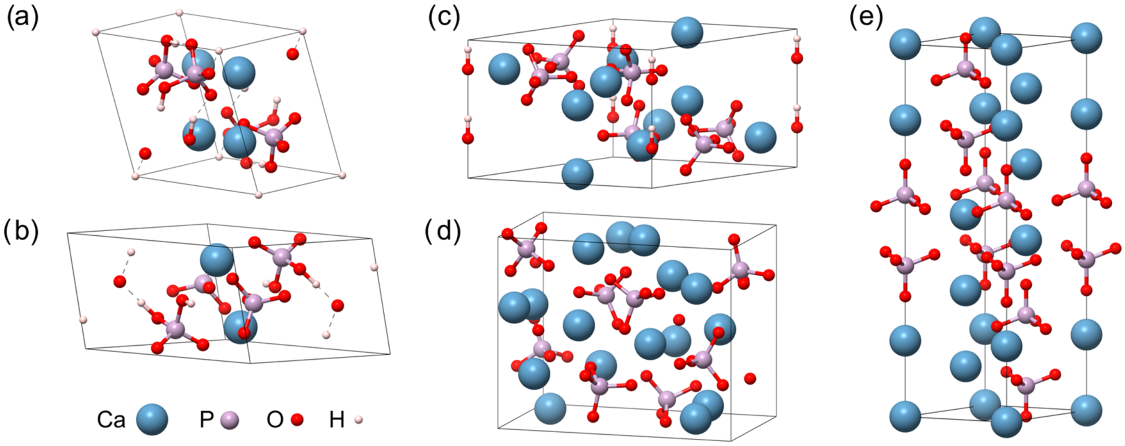

Figure 1. Unit cell representation of pristine (nonsubstituted) phases for the apatite-based materials: (a) $CaHPO_4$, (b) $Ca(H_2PO_4)_2$, (c) $Ca_{10}(PO_4)_6(OH)_2$, (d) $Ca_4(PO_4)_2O$, and (e) γ-$Ca_3(PO_4)_2$. Light blue, pink, red, and white spheres represent Ca, P, O, and H atoms, respectively.

$(H_2PO_4)_2$, Ca/P = 0.50),[24] dicalcium phosphate anhydrous ($CaHPO_4$, Ca/P = 1.00),[25] tricalcium phosphate (γ-$Ca_3(PO_4)_2$, Ca/P = 1.50),[26] and tetracalcium phosphate ($Ca_4(PO_4)_2O$, Ca/P = 2.00).[27] Consequently, the unique morphologies and distributions of surface active sites intrinsic to these phases may be investigated to enhance the performance of HAP-based materials, in particular catalytic reactions.

In this study, we investigate the variations in the Ca/P molar ratio along with ionic substitutions to determine whether the effects of substitutions are contingent on the Ca/P ratio or remain uniform across different crystallographic phases. To achieve this objective, we performed density functional theory (DFT) calculations to explore the energetic, electronic, and structural implications of ionic substitution within various HAP phases. Using Spearman's correlation analysis, we investigated the most important factors that affect the physicochemical stability of apatite-based materials. Our results provide valuable information on the tunable properties of HAP and its potential aptitude for tailored catalytic applications, thus contributing to the formulation of sustainable and economically viable catalysts.

2. THEORETICAL APPROACH AND COMPUTATIONAL DETAILS

2.1. Total Energy Calculations. Our first-principles calculations are based on spin-polarized DFT[28,29] within the Perdew−Burke−Ernzenhof (PBE) formulation[30] for the exchange-correlation energy functional, as implemented in the Vienna *ab initio* simulation package (VASP),[31,32] version 5.4.4. The all-electron projected augmented-wave (PAW) method[33,34] was used to describe core−valence electron interactions, and the Kohn−Sham (KS) equations were solved with KS states expanded in plane waves.

For relaxation of the lattice parameters and atomic positions, a plane-wave cutoff energy of 869 eV was used to ensure accurate convergence of the stress tensor, which shows slow convergence as a function of the number of plane waves. All remaining calculations used a cutoff energy of 548 eV, which is 12.5% higher than the highest recommended value for the chemical elements in the bulk materials. The integration of the Brillouin zone (BZ) was sampled using a Monkhorst−Pack[35] **k**-mesh of 2 × 2 × 3, which was increased to 4 × 4 × 6 for the density of states (DOS) calculations to obtain accurate results. For free atom calculations, an orthorhombic box of dimensions 20 × 21 × 22 Å was used, which is necessary to avoid spherical symmetry in the electron density, while the integration of the BZ was performed using only the Γ-point due to the lack of dispersion in the electronic states. The equilibrium structures were obtained using a force convergence threshold of 0.025 eV $Å^{-1}$ on each atom and a global energy convergence criterion of 10^{-5} eV. Additional details on the selected PAW projectors, computational parameters, and convergence tests are provided in the Supporting Information file.

2.2. Selecting Functional Ionic Substituents. We selected ionic species for chemical substitutions that preserved the stoichiometric charge of the unit cells, i.e., the electron counting rule was based on the oxidation state of the chemical species. In addition, we limited our selection of tetroxides to species that maintained the same number of atoms when replacing the PO_4^{3-} groups, preventing significant structural modifications. Based on these criteria, we selected the following species: X = Mg^{2+}, Sr^{2+}, Ba^{2+}, Zn^{2+}, and Cd^{2+} to replace Ca^{2+} sites; Y = As and V to replace phosphorus at PO_4^{3-} sites; and Z = F^-, Cl^-, and Br^- to replace OH^- sites. This selection resulted in 72 structures corresponding to the Ca/P ratio of 1.67, together with 18 structures for each phase that exhibit varying Ca/P molar ratios. In total, we considered a set of 144 structures for the purpose of conducting equilibrium optimizations through stress-tensor calculations.

2.3. Structure Configurations. The initial configuration of the hexagonal HAP bulk unit cell, with a Ca/P molar ratio of 1.67, was obtained from experimental measurements.[37] To maintain the exact stoichiometry, we reduced the space group from $P6_3/m$ to $P6_3$. This approach has been successfully applied in previous computational studies.[38,39] Substituted HAP-based structures were created by replacing all atoms at the specific sites of Ca^{2+}, PO_4^{3-}, and OH^- in the pure $P6_3$ HAP structure, resulting in mono-, di-, and trisubstituted materials.

For the remaining apatite phases with different ratios of Ca/P, Figure 1, we maintained the space group consistent with the experimental characterization. Initial configurations for Ca/P ratios of 0.50, 1.00, 1.50, and 2.00 were based on the structures of $Ca(H_2PO_4)_2$,[24] $CaHPO_4$,[25] γ-$Ca_3(PO_4)_2$,[26] and $Ca_4(PO_4)_2O$,[27] respectively. Since these phases lack hydroxyl sites, our evaluation of apatite-based materials only considered substitutions at the Ca^{2+} and PO_4^{3-} sites.

Table 1. DFT Results Obtained for the Structural, Energetic, and Electronic Properties of the Pristine (Nonsubstituted) Phases for the Apatite-Based Materials: Ca/P Molar Ratios, Lattice Parameters (a_0, b_0, c_0), Cohesive Energy (E_{coh}), and Fundamental Energy Bandgap at the Γ-Point (E_g)[a][24,26,27,36,37]

apatite systems	space group	Ca/P	a_0 (Å)	b_0 (Å)	c_0 (Å)	E_{coh} (eV)	E_g^{Γ} (eV)
$Ca(H_2PO_4)_2$	$P\bar{1}$	0.50	8.99 (7.56)	8.15 (8.25)	5.55 (5.55)	−4.74	5.16
$CaHPO_4$	$P\bar{1}$	1.00	6.71 (6.72)	6.98 (6.98)	7.09 (7.10)	−5.24	5.44
γ-$Ca_3(PO_4)_2$	$R\bar{3}m$	1.50	5.31 (5.25)	5.31 (5.25)	18.77 (18.67)	−5.71	5.53
$Ca_{10}(PO_4)_6(OH)_2$	$P6_3$	1.67	9.55 (9.42)	9.55 (9.42)	6.89 (6.87)	−5.63	5.28
$Ca_4(PO_4)_2O$	$P2_1$	2.00	7.06 (7.02)	12.07 (11.99)	9.54 (9.47)	−5.72	4.54

[a] Experimental results[24,26,27,36,37] are presented within parentheses.

3. RESULTS AND DISCUSSION

3.1. Pristine Apatite-Based Materials. In this section, we will summarize the most important findings related to the pristine apatite phases and compare our results with experimental data.

3.1.1. Structure Features and Parameters. The structural properties of the pristine (nonsubstituted) phases are summarized in Table 1, where we also present the structural characteristics of the calcium phosphate compounds examined in this study. HAP and γ-tricalcium phosphate both crystallize in hexagonal unit cells, although with different space groups and the number of formula units per cell. HAP belongs to the $P6_3$ space group with two formula units per cell, while γ-tricalcium phosphate adopts the $R\bar{3}m$ space group with three formula units per unit cell. Monocalcium phosphate and dicalcium phosphate anhydrous crystallize in triclinic unit cells within the $P\bar{1}$ space group. However, they differ in the number of formula units per cell: $Ca(H_2PO_4)_2$ contains two, while $CaHPO_4$ accommodates four. Tetracalcium diphosphate monoxide stands out as the only compound in this study with a monoclinic unit cell, crystallizing in the $P2_1$ space group with four formula units per cell. Based on our analysis, the primary structural characteristics of these phases can be summarized as follows:

1. **Hydroxyapatite:** Contains two distinct Ca cation sites. Ca(I) comprises four atoms arranged in two columns on opposite sides of the unit cell, with two cations in each column. Ca(II) consists of six atoms arranged in two parallel equilateral triangles. The PO_4^{3-} groups form two equilateral triangles coplanar with the Ca(II) triangles but with larger edges. Hydroxyl groups align vertically in the center of both Ca(II) and PO_4^{3-} triangles, slightly offset from their planes.[40]
2. **Monocalcium phosphate:** The PO_4 sites are aligned parallel to the [010] direction. All calcium atoms are crystallographically equivalent, each coordinated to eight oxygen atoms and organized in layers parallel to the direction [100], bonded by five different hydrogen bonds.
3. **Dicalcium phosphate anhydrous:** Features two types of Ca cations. Ca(I) is coordinated with seven oxygen atoms in a pentagonal bipyramidal arrangement, while Ca(II) is coordinated with eight oxygen atoms. Distorted Ca-PO_4 chains align in planes parallel to the [010] direction, a feature shared with other calcium phosphates such as $Ca(H_2PO_4)_2{\cdot}H_2O$.[36]
4. **γ-Tricalcium phosphate:** Contains two types of Ca atoms arranged in planes parallel to the [001] direction. Ca(I) occupies $\bar{3}m$ symmetry sites and coordinates with 12 oxygen atoms, while Ca(II) coordinates with ten. The structure can be described as a linear sequence of parallel $PO_4 - Ca(II) - Ca(I) - Ca(II) - PO_4$ chains repeating along the b_0 direction.[26]
5. **Tetracalcium diphosphate monoxide:** Contains eight crystallographically distinct Ca atoms. Ca(I) through Ca(V), along with Ca(VII) and Ca(VIII), each coordinates with seven oxygen atoms, while Ca(VI) coordinates with eight. The phosphate groups are also crystallographically distinct, with each oxygen in all phosphate groups coordinating to three Ca cations. This phase uniquely contains oxide anions strongly coordinated to Ca atoms, which were not substituted in this study due to their absence in the other phases examined.

Table 1 presents a comparison between our calculated equilibrium lattice parameters and experimental results for various Ca/P ratios. The analysis reveals distinct patterns across different phases: (i) For Ca/P = 1.67, 1.50, and 2.00, these phases exhibited slight expansions in all lattice parameters compared to experimental values. The most significant deviation was observed in the HAP (Ca/P = 1.67) structure, where the $a_0 = b_0$ vectors expanded by 1.38%. (ii) For the Ca/P = 0.50 phase, the lattice parameter a_0 exhibited the most significant deviation, expanding by 18.92% compared to experimental results. This pronounced discrepancy is consistent with findings from the Materials Project database,[41] which also references the same initial apatite structure and reports a similar deviation from the experimental data. However, when comparing our calculated value a_0 with the theoretical results from the Materials Project database, the deviation decreases to 7.28%. This smaller difference highlights the impact of methodological variations between the two studies. In contrast to a_0, the lattice parameter b_0 expanded by only 1.21%, and the parameter c_0 remained unchanged. (iii) For Ca/P = 1.00, the relaxed structure for this phase demonstrated excellent agreement with the experimental values, with minimal deviations observed.

These variations in the lattice parameters for different ratios Ca/P suggest that the computational approach may have varying degrees of effectiveness in capturing the structural nuances of each phase. In general, with the exception of the phase Ca/P = 0.50, our calculations provided a reasonably accurate representation of the experimental lattice parameters, lending confidence to the structural basis of our subsequent analyzes.

3.1.2. Stability and Electronic Properties. The cohesive energy (E_{coh}), which is calculated as the energy difference between the total energy (E_{tot}^{bulk}) and the cumulative sum of the total energies of the free atoms (E_{tot}^{i}). Consequently, it can be expressed by the following equation,

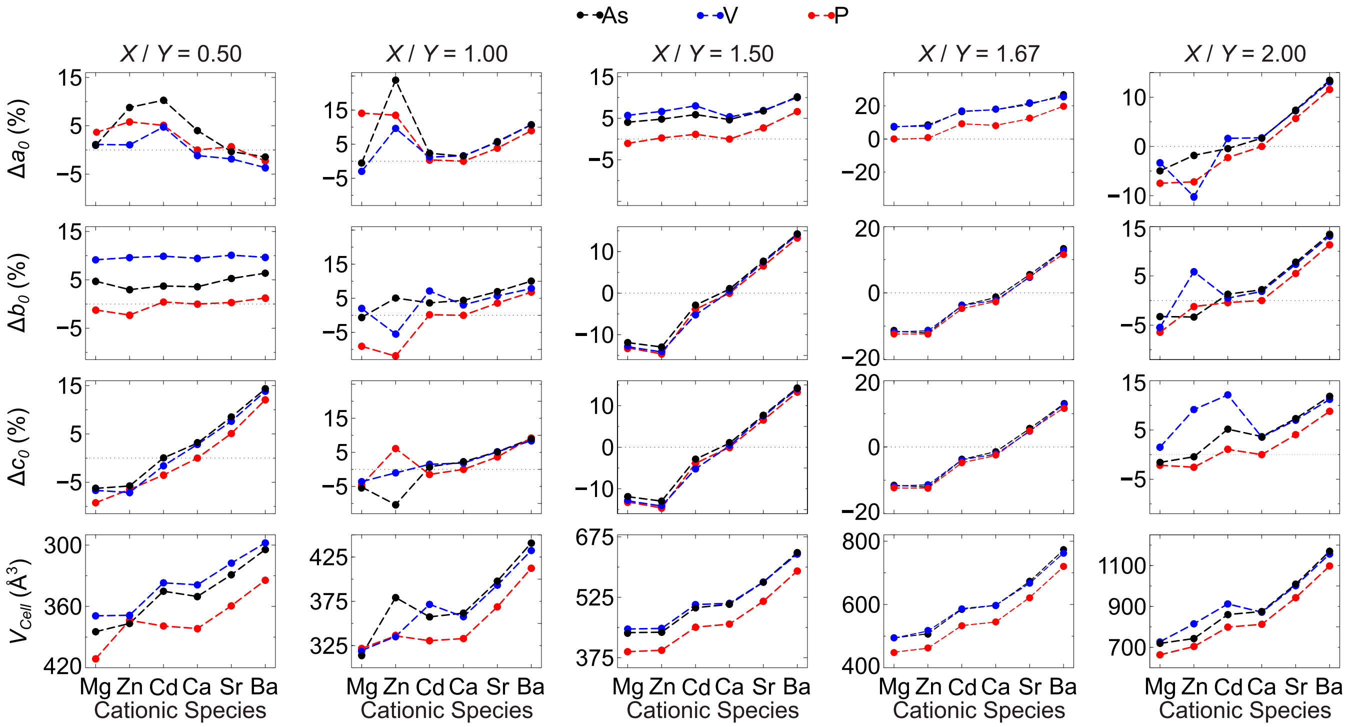

Figure 2. Structural properties of substituted apatite-like materials: variation of lattice parameters (Δa_0, Δb_0, and Δc_0) calculated as percentage changes relative to the pure apatite structure and volume of the unit cell (V_{cell}).

$$E_{\text{coh}} = \frac{(E_{\text{tot}}^{\text{bulk}} - \sum_i N^i E_{\text{tot}}^i)}{N_{\text{tot}}} \tag{1}$$

where N^i is the number of atoms of chemical element i and N_{tot} is the total number of atoms in the bulk unit cell. Thus, based on its definition, E_{coh} is a key stability indicator, measuring the energy required to split a solid into free atoms. Its magnitude reflects the bonding strength, and higher values indicate strong atomic interactions and improved stability, durability, and decomposition resistance.

As shown in Table 1, $Ca_4(PO_4)_2O$ and γ-$Ca_3(PO_4)_2$ are the most stable pure apatite materials, with E_{coh} values of −5.72 and −5.71 eV, respectively. In contrast, the Ca/P = 0.50 phase ($Ca(H_2PO_4)_2$) exhibits the lowest stability, with $E_{\text{coh}} = -4.74$ *eV*, which is 20.67% higher than that of $Ca_4(PO_4)_2O$. These results suggest that the higher Ca/P ratios generally correspond to more stable apatite structures.

The fundamental energy bandgap at the Γ-point (E_g, in eV), was evaluated using the following equation,

$$E_g = E_{\text{CBM}}^{\Gamma} - E_{\text{VBM}}^{\Gamma} \tag{2}$$

where E_{CBM}^{Γ} and E_{VBM}^{Γ} are the energies of the conduction band minimum and valence band maximum at the Γ-point, respectively. Therefore, this analysis facilitates the determination of whether the material exhibits conductive, semiconductive, or insulating behavior, which is important to drive its application.

According to the results summarized in Table 1, all pristine apatites exhibit insulating characteristics, as evidenced by their high values of E_g. The γ-tricalcium phosphate phase (Ca/P = 1.50) has the largest band gap, which is 21.81% higher than the lowest value E_g observed in the structure Ca/P = 2.00. Our calculated E_g values are generally consistent with other theoretical investigations available in the Materials Project library.[42] The largest observed deviation was approximately 8.67% for the Ca/P = 1.00 phase. In general, the high band gap energies confirm the insulating nature of the studied apatite materials, with the γ-tricalcium phosphate phase exhibiting the most pronounced insulating character.

3.2. Effects of Ionic Substitution in Apatite-Based Materials.

In this section, we present a comprehensive analysis of the impacts resulting from ionic substitution on the energetic, electronic, and structural properties.

3.2.1. Equilibrium Lattice Parameters. The lattice parameter variations (Δa_0, Δb_0, and Δc_0) were calculated as percentage changes relative to the pristine apatite structures using the following equation

$$\Delta x_0 = 100\frac{(x_0^i - x_0^{\text{ref}})}{x_0^{\text{ref}}} \tag{3}$$

where $x = a, b, c$, $x_0{}^i$ represents the equilibrium lattice constant of the substituted apatite-like material, and $x_0{}^{\text{ref}}$ is the equilibrium lattice of the pristine apatite.

As shown in Figure 2, the variation of the lattice parameters and the corresponding cell volume (V_{cell}) fluctuate in response to variations in the radii of the cationic and anionic substitution species, which is consistent with size effects. Larger cations (e.g., Sr^{2+}, Ba^{2+}) and anions (e.g., $AsO_4{}^{3-}$, $VO_4{}^{3-}$) lead to an expansion of V_{cell}, while smaller species (e.g., Mg^{2+}, Zn^{2+}, $PO_4{}^{3-}$) generally result in volume contraction.

Interestingly, the hexagonal phases (Ca/P = 1.50 and 1.67) exhibit unique behavior: the a_0 parameter does not contract with any substitutional species, even when the smallest cations are introduced, while $b_0 = c_0$ prove to be more flexible. For the Ca/P = 0.50 phase, the smaller cations (e.g., Mg^{2+}, Zn^{2+}, Cd^{2+}) increase the a_0 lattice parameter, whereas the larger cations have the opposite effect. Furthermore, phosphate species have a more

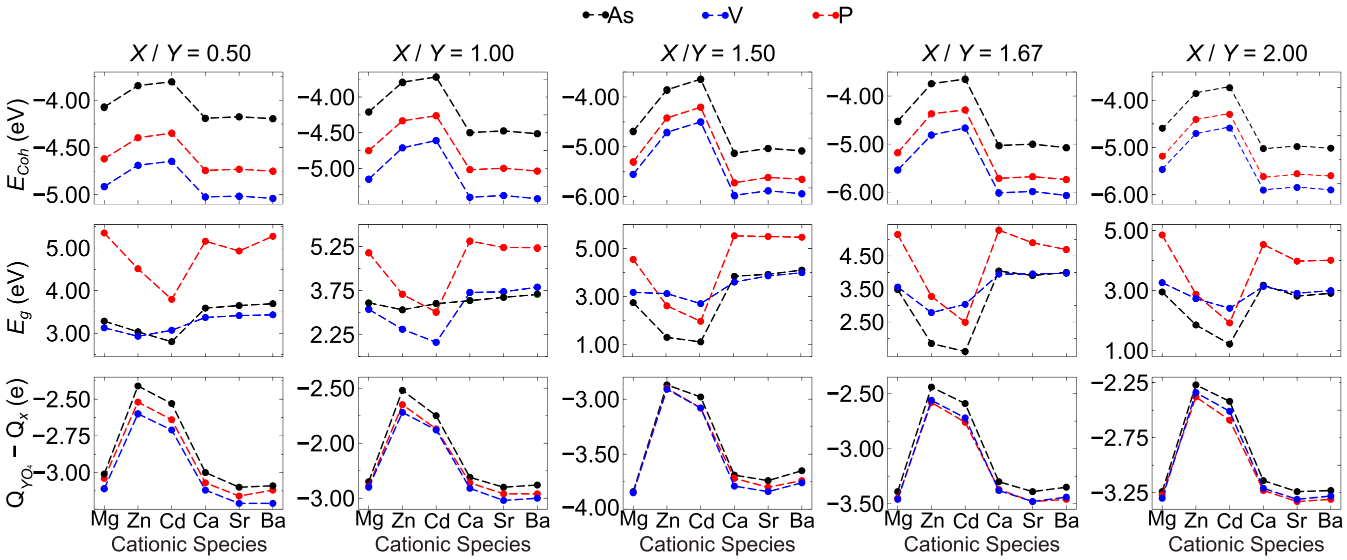

Figure 3. Energetic and electronic properties of substituted apatite-like materials: cohesive energy per atom (E_{coh}), fundamental energy bandgap at the Γ-point (E_{g}), and net atomic charge difference between anionic and cationic species within the bulk structure ($Q_{YO_4} - Q_X$).

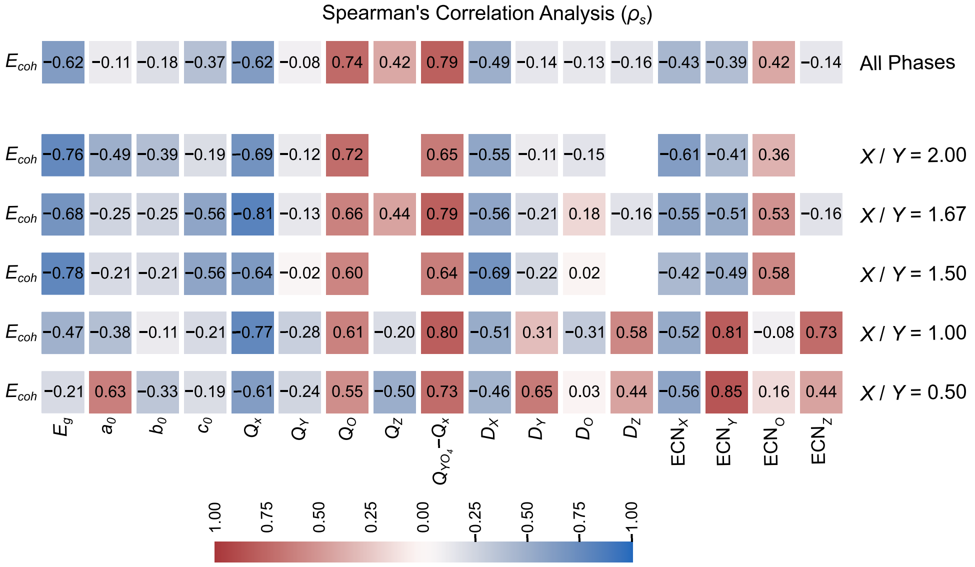
Spearman's Correlation Analysis (ρ_s)

	E_g	a_0	b_0	c_0	Q_X	Q_Y	Q_O	Q_Z	$Q_{YO_4}-Q_X$	D_X	D_Y	D_O	D_Z	ECN_X	ECN_Y	ECN_O	ECN_Z	
E_{coh}	−0.62	−0.11	−0.18	−0.37	−0.62	−0.08	0.74	0.42	0.79	−0.49	−0.14	−0.13	−0.16	−0.43	−0.39	0.42	−0.14	All Phases
E_{coh}	−0.76	−0.49	−0.39	−0.19	−0.69	−0.12	0.72		0.65	−0.55	−0.11	−0.15		−0.61	−0.41	0.36		X / Y = 2.00
E_{coh}	−0.68	−0.25	−0.25	−0.56	−0.81	−0.13	0.66	0.44	0.79	−0.56	−0.21	0.18	−0.16	−0.55	−0.51	0.53	−0.16	X / Y = 1.67
E_{coh}	−0.78	−0.21	−0.21	−0.56	−0.64	−0.02	0.60		0.64	−0.69	−0.22	0.02		−0.42	−0.49	0.58		X / Y = 1.50
E_{coh}	−0.47	−0.38	−0.11	−0.21	−0.77	−0.28	0.61	−0.20	0.80	−0.51	0.31	−0.31	0.58	−0.52	0.81	−0.08	0.73	X / Y = 1.00
E_{coh}	−0.21	0.63	−0.33	−0.19	−0.61	−0.24	0.55	−0.50	0.73	−0.46	0.65	0.03	0.44	−0.56	0.85	0.16	0.44	X / Y = 0.50

Figure 4. Spearman's correlation analysis (ρ_s) of the cohesive energy per atom (E_{coh}) for the of substituted apatite-like materials in relation to the following properties: energy gap at the Γ-point (E_{g} in eV), length of lattice parameters (a_0, b_0, and c_0 in Å), average net atomic charges (Q_X, Q_Y, Q_O, and Q_Z in e), net atomic charge difference between anionic and cationic species ($Q_{YO_4} - Q_X$ in e), average distance for nearest neighbors (D_X, D_Y, D_O, and D_Z in Å), and effective coordination number (ECN_X, ECN_Y, ECN_O, and ECN_Z in NNN). Subscripts are defined as X = Ca, Mg, Sr, Ba, Zn, and Cd; Y = P, As, and V; and Z = H, F, Cl, and Br. Direct and inverse monotonic correlations are observed when ρ_s is closer to 1 and −1, respectively.

pronounced influence on the b_0 lattice parameter, while the c_0 parameter behaves as expected for this phase.

3.2.2. Effects of Ionic Substitution on the Structural Stability. Two notable trends are observed for all structures: the stability (cohesive energy analyzes) of apatite-based materials (i) decreased with substitutions by d-block elements such as Zn and Cd, and (ii) increased in order of $AsO_4 < PO_4 < VO_4$ tetroxide substituents. Figure 3 shows that the presence of d-block elements in the apatite structure leads to a decrease in the fundamental energy band gap, which can be partially explained by the principle of maximum hardness.[43] This principle suggests that materials with smaller E_{g} tend to exhibit fewer ionic interactions and higher reactivity.

Consequently, substitution with Zn and Cd reduced the ionic nature of the bulk structures. This effect can be observed by the difference between the average charge of YO_4 groups and the average charge of X cations ($Q_{YO_4} - Q_X$). The weaker ionic interactions induced by these d-block elements lead to reduced charge differences and weaker atomic bonds, resulting in decreased structural stability.

In contrast, substitutions with alkaline earth cations, such as Sr^{2+} and Ba^{2+} tend to restore stronger ionic interactions, thus increasing charge differences and improving structural stability. This is due to the higher ionic character of alkaline earth cations compared to d-block elements, which promotes a more polarized bonding with oxygen atoms. The correlation between E_{coh} and $Q_{YO_4} - Q_X$ indicates a strong relationship between the

https://doi.org/10.1021/acsomega.4c09997

type of cationic substituent, the charge difference, and the structural stability of these materials. This trend has been further confirmed through a Spearman's correlation analysis, as discussed in Section 4.

Furthermore, tetroxide substituents (VO_4, PO_4, AsO_4) can influence structural stability in different ways. The stability order of $AsO_4 < PO_4 < VO_4$ cannot be solely explained by the E_g values, as VO_4-substituted bulks exhibit the highest stability despite not having the largest band gaps. To understand this behavior, we performed local DOS calculations. These calculations reveal significant d-p hybridization between the d-orbitals of the Y atoms (e.g., V, P, As) and the p-orbitals of the oxygen atoms. This hybridization, particularly pronounced for VO_4, leads to a stronger covalent character in the bonds and contributes to the enhanced stability of these phases.[44,45] Not surprisingly, the intensity of the d-p hybridization correlates well with the cohesive energy (E_{coh}), highlighting the strong relationship between the bulk electronic structure and the stability of substituted apatite materials.

It is important to note that, in addition to thermodynamic stability, other factors play a crucial role in practical ion exchange for real-world applications. In particular, ion conductivity, ion mobility, and the kinetics of ion exchange can significantly influence the feasibility of synthesizing substituted apatites experimentally. These properties depend on diffusion rates within the apatite lattice, which can be impacted by ion migration barriers and structural distortions induced by substitutions. While our study primarily focuses on thermodynamic aspects, experimental research has demonstrated that the substituted apatites investigated here not only exhibit thermodynamic stability but also exhibit promising properties for practical applications across different fields.[46−50]

4. INSIGHTS INTO ENERGETIC STABILITY FROM SPEARMAN'S CORRELATION

To improve our understanding of the key factors that contribute to the stability of apatite-like materials, we performed a Spearman rank correlation analysis. Our analysis was carried out on all optimized bulk structures, both collectively and grouped by their composition X/Y ratios (e.g., 0.50, 1.00, 1.50, etc.). The primary objective was to identify the correlations among the structural, energetic, and electronic properties selected in this study. Figure 4 presents the results as a correlation matrix, where each cell represents the correlation coefficient (ρ_s) between the cohesive energy (E_{coh}) of a specific phase (rows) and the studied properties (columns). The strength of the correlation increases as ρ_s approaches 1 (indicating a direct correlation) or −1 (indicating an inverse correlation). The analysis yielded several critical insights into the determinants of structural stability:

- Charges: Q_X, Q_O, and $Q_{YO_4} - Q_X$ exhibited strong correlations with E_{coh}, confirming the discussions in Section 3.2.1. The negative ρ_s for Q_X indicate that stability increases with more highly charged cations, while the opposite holds for Q_O. Conversely, $|\rho_s| \leq 0.30$ for Q_Y confirms that Y had minimal impact on the ionic nature.
- E_g: This property can be used as a stability descriptor for X/Y ratios of 1.50, 1.67, and 2.00, as discussed in Section 3.2.1. However, its effect is less pronounced for the triclinic phases with X/Y ratios of 0.50 and 1.00.
- Structural properties: ECN_Y (average effective number of Y substituents) and ECN_H (average effective number of H) showed the highest ρ_s among structural properties, particularly for X/Y ratios of 0.50 and 1.00. However, the standard deviations were lower than 0.1 for both properties and phases, indicating that substitutions by the chosen ions did not significantly affect these parameters. Therefore, the selected structural properties are poor descriptors of the cohesive energy of the selected apatite-like compounds.

Thus, only 9.4% (42.7%) of the explored properties demonstrated strong correlations with $|\rho_s| > 0.75$ (moderate correlations with $|\rho_s| > 0.50$). The predominance of weak correlations, indicated by the fact that most absolute coefficients fall below 0.50, underscores the complex interplay of factors that affect the stability of the selected apatites. This complexity highlights the challenge of isolating definitive determinants of stability, suggesting that energetic stability results from a multifaceted combination of structural, chemical, and electronic contributions rather than being governed by a singular property.

5. CONCLUSIONS

In this investigation, we performed DFT-PBE calculations to characterize the physicochemical properties of apatite-like materials as a function of the Ca/P ratios, ranging from 0.50 to 2.00. Apatite-like materials show variations in space group, composition, size, and stability, and hence their physicochemical properties spread over a wide range of values. Our aim was to explore the impact of ionic substitutions at the cationic and anionic sites on the geometric, electronic, and energetic characteristics of these materials. Furthermore, we used Spearman correlation analysis to discern the primary factors (descriptors) that influence the stability and material properties.

Structurally, we identified a strong correlation between the ionic radii of the substituents and the unit cell volume. Substitutions with larger cations, such as Ba^{2+} and Sr^{2+}, resulted in expansions of the volume of the unit cells, while smaller cations, such as Mg^{2+} and Cd^{2+}, led to volume contractions. Stability analysis revealed that substitutions with Zn and Cd significantly reduced the magnitude of the cohesive energies, indicating decreased material stability. This decline in stability correlated with a narrowing of the fundamental band gap at the Γ-point and a reduction in ionic character, quantified by the charge difference between the net atomic charges of YO_4 groups and X cations ($Q_{YO_4} - Q_X$). Among the tetroxide substituents, VO_4 was the most stable, followed by PO_4 and AsO_4. This trend is attributed to the extent of d-p hybridization between the d-orbitals of Y atoms and the p-orbitals of oxygen, which closely matched the cohesive energy order.

Finally, Spearman's correlation analysis further highlighted that net atomic charges on the X and O species, along with the energy gap, have a significant influence on the cohesive energy. This analysis underscores the importance of electronic properties in determining material stability. Overall, our findings provide valuable insight into the impact of ionic substitutions on the stability of apatite-like materials, contributing to a deeper understanding of their properties.

■ ASSOCIATED CONTENT

Supporting Information

The Supporting Information is available free of charge at https://pubs.acs.org/doi/10.1021/acsomega.4c09997.

Data used for the figures, as well as additional analyses and additional computational parameters used in the calculations (PDF)

AUTHOR INFORMATION

Corresponding Author

Juarez L. F. Da Silva − *São Carlos Institute of Chemistry, University of São Paulo, 13560-970 São Carlos, SP, Brazil;* orcid.org/0000-0003-0645-8760;
Email: juarez_dasilva@iqsc.usp.br

Authors

Henrique S. Marques − *Institute of Mathematics and Computer Sciences, University of São Paulo, 13566-590 São Carlos, SP, Brazil*

Albert F. B. Bittencourt − *Institute of Science and Technology, Federal University of Jequitinhonha and Mucuri Valleys, 39100-000 Diamantina, MG, Brazil; São Carlos Institute of Chemistry, University of São Paulo, 13560-970 São Carlos, SP, Brazil;* orcid.org/0000-0002-9418-0166

Complete contact information is available at:
https://pubs.acs.org/10.1021/acsomega.4c09997

Funding

The Article Processing Charge for the publication of this research was funded by the Coordenacao de Aperfeicoamento de Pessoal de Nivel Superior (CAPES), Brazil (ROR identifier: 00x0ma614).

Notes

The authors declare no competing financial interest.

ACKNOWLEDGMENTS

The authors appreciate the support from FAPESP (São Paulo Research Foundation) and Shell, grant numbers 2017/11631-2 and 2018/21401-7, and the strategic importance of the support given by ANP (Brazil's National Oil, Natural Gas and Biofuels Agency) through the R&D levy regulation. HSM and AFBB also acknowledge the financial support of FAPESP, grant numbers 2017/11937-4, 2021/05697-6, and 2022/12778-5. The authors thank the reviewers for their insightful feedback and constructive suggestions, which have greatly improved the quality of the manuscript. The authors extend their deep appreciation for the essential contributions of both the Department of Information Technology at Campus São Carlos and the National Laboratory for Scientific Computing (LNCC/MCTI, Brazil) − Santos Dumont, which were instrumental in achieving the results reported in this article.

REFERENCES

(1) Diallo-Garcia, S.; Osman, M. B.; Krafft, J.-M.; Casale, S.; Thomas, C.; Kubo, J.; Costentin, G. Identification of Surface Basic Sites and Acid-Base Pairs of Hydroxyapatite. *J. Phys. Chem. C* **2014**, *118*, 12744−12757.

(2) Ben Osman, M.; Diallo-Garcia, S.; Herledan, V.; Brouri, D.; Yoshioka, T.; Kubo, J.; Millot, Y.; Costentin, G. Discrimination of Surface and Bulk Structure of Crystalline Hydroxyapatite Nanoparticles by NMR. *J. Phys. Chem. C* **2015**, *119*, 23008−23020.

(3) Osman, M. B.; Krafft, J.-M.; Thomas, C.; Yoshioka, T.; Kubo, J.; Costentin, G. Importance of the Nature of the Active Acid/Base Pairs of Hydroxyapatite Involved in the Catalytic Transformation of Ethanol to n-Butanol Revealed by Operando DRIFTS. *ChemCatChem* **2019**, *11*, 1765−1778.

(4) Mori, K.; Hara, T.; Oshiba, M.; Mizugaki, T.; Ebitani, K.; Kaneda, K. Catalytic Investigations of Carbon-Carbon Bond-Forming Reactions by a Hydroxyapatite-Bound Palladium Complex. *New J. Chem.* **2005**, *29*, 1174−1181.

(5) Elazarifi, N.; Ezzamarty, A.; Leglise, J.; Ménorval, L.-C. d.; Moreau, C. Kinetic Study of the Condensation of Benzaldehyde with Ethylcyanoacetate in the Presence of Al-Enriched Fluoroapatites and Hydroxyapatites as Catalysts. *Appl. Catal., A* **2004**, *267*, 235−240.

(6) Opre, Z.; Grunwaldt, J.-D.; Mallat, T.; Baiker, A. Selective Oxidation of Alcohols with Oxygen on Ru-Co-Hydroxyapatite: A Mechanistic Study. *J. Mol. Catal. A:Chem.* **2005**, *242*, 224−232.

(7) Fihri, A.; Len, C.; Varma, R. S.; Solhy, A. Hydroxyapatite: A Review of Syntheses, Structure and Applications in Heterogeneous Catalysis. *Coord. Chem. Rev.* **2017**, *347*, 48−76.

(8) Sheldon, R. A. Fundamentals of Green Chemistry: Efficiency in Reaction Design. *Chem. Soc. Rev.* **2012**, *41*, 1437−1451.

(9) Kiani, D.; Baltrusaitis, J. Surface Chemistry of Hydroxyapatite for Sustainable n-Butanol Production from Bio-Ethanol. *Chem. Catal.* **2021**, *1*, 782−801.

(10) Li, S.; Li, Y.; Shen, W.; Bai, Y.; Kong, L. Hydroxyapatite-Based Catalysis in Environmental Decontamination. *J. Cleaner Prod.* **2022**, *380*, No. 134961.

(11) Jiang, Y.; Yuan, Z.; Huang, J. Substituted Hydroxyapatite: A Recent Development. *Mater. Technol.* **2020**, *35*, 785−796.

(12) Gong, B.; Su, T.; Xie, X.; Ji, H.; Qin, Z. Promotional Effects of Mg-Substituted Ni/MgxHAP Catalysts on Carbon Resistance during Dry Reforming of Methane. *Ind. Eng. Chem. Res.* **2023**, *62*, 12935−12948.

(13) Seelam, P. K.; Balla, P.; Rajendiran, R.; Ravi, B.; Prathap, C.; Lassi, U.; Kim, S.; Vijayanand, P. Activity of Nickel Supported Over Nanorod-Shaped Strontium Hydroxyapatite Catalysts in Selective Methanation of CO & CO_2. *Top. Catal.* **2023**, *66*, 1391−1405.

(14) Ratnayake, J. T. B.; Mucalo, M.; Dias, G. J. Substituted Hydroxyapatites for Bone Regeneration: A Review of Current Trends. *J. Biomed. Mater. Res.* **2017**, *105*, 1285−1299.

(15) Ezerskyte-Miseviciene, A.; Bogdanoviciene, I.; Zilinskas, A.; Beganskiene, A.; Kareiva, A. Synthesis, Characterization and Investigation of Catalytic Properties of Metal-Substituted (M = Mg^{2+}, Zn^{2+} and Na^+) Calcium Hydroxyapatite. *J. Aust. Ceram. Soc.* **2020**, *56*, 839−848.

(16) Lovón-Quintana, J. J.; Rodriguez-Guerrero, J. K.; Valença, P. G. Carbonate Hydroxyapatite as a Catalyst for Ethanol Conversion to Hydrocarbon Fuels. *Appl. Catal., A* **2017**, *542*, 136−145.

(17) Zhu, Y.; Zhang, X.; Long, F.; Liu, H.; Qian, M.; He, N. Synthesis and Characterization of Arsenate/Phosphate Hydroxyapatite Solid Solution. *Mater. Lett.* **2009**, *63*, 1185−1188.

(18) Sugiyama, S.; Osaka, T.; Hirata, Y.; Sotowa, K. Enhancement of the Activity for Oxidative Dehydrogenation of Propane on Calcium Hydroxyapatite Substituted with Vanadate. *Appl. Catal., A* **2006**, *312*, 52−58.

(19) Yook, H.; Hwang, J.; Yeo, W.; Bang, J.; Kim, J.; Kim, T. Y.; Choi, J.-S.; Han, J. W. Design Strategies for Hydroxyapatite-Based Materials to Enhance Their Catalytic Performance and Applicability. *Adv. Mater.* **2023**, *35*, No. 2204938.

(20) Ho, C. R.; Zheng, S.; Shylesh, S.; Bell, A. T. The Mechanism and Kinetics of Methyl Isobutyl Ketone Synthesis from Acetone over Ion-Exchanged Hydroxyapatite. *J. Catal.* **2018**, *365*, 174−183.

(21) Ramesh, K.; Ling, E. G. Y.; Gwie, C. G.; White, T. J.; Borgna, A. Structure and Surface Reactivity of WO_4^{2-}, SO_4^{2-}, PO_4^{3-} Modified Ca-Hydroxyapatite Catalysts and Their Activity in Ethanol Conversion. *J. Phys. Chem. C* **2012**, *116*, 18736−18745.

(22) Akri, M.; Zhao, S.; Li, X.; Zang, K.; Lee, A. F.; Isaacs, M. A.; Xi, W.; Gangarajula, Y.; Luo, J.; Ren, Y.; Cui, Y.-T.; Li, L.; Su, Y.; Pan, X.; Wen, W.; Pan, Y.; Wilson, K.; Li, L.; Qiao, B.; Ishii, H.; Liao, Y.-F.; Wang, A.; Wang, X.; Zhang, T. Atomically Dispersed Nickel as Coke-Resistant Active Sites for Methane Dry Reforming. *Nat. Commun.* **2019**, *10*, No. 5181.

(23) Gadipelly, C.; Deshmukh, G.; Mannepalli, L. K. Transition Metal Exchanged Hydroxyapatite/Fluorapatite Catalysts for C−C and C−N Bond Forming Reactions. *Chem. Rec.* **2021**, *21*, 1398−1416.

(24) Dickens, B.; Prince, E.; Schroeder, L. W.; Brown, W. E. $Ca(H_2PO_4)_2$, a Crystal Structure Containing Unusual Hydrogen Bonding. *Acta Crystallogr. B* **1973**, *29*, 2057−2070.

(25) Dickens, B.; Bowen, J. S.; Brown, W. E. A Refinement of the Crystal Structure of $CaHPO_4$ (Synthetic Monetite). *Acta Crystallogr. B* **1972**, *28*, 797−806.

(26) Sugiyama, K.; Tokonami, M. Structure and Crystal Chemistry of a Dense Polymorph of Tricalcium Phosphate $Ca_3(PO_4)_2$: A Host to Accommodate Large Lithophile Elements in the Earth's Mantle. *Phys. Chem. Miner.* **1987**, *15*, 125−130.

(27) Dickens, B.; Brown, W. E.; Kruger, G. J.; Stewart, J. M. $Ca_4(PO_4)_2O$, Tetracalcium Diphosphate Monoxide. Crystal structure and Relationships to $Ca_5(PO_4)_3OH$ and $K_3Na(SO_4)_2$. *Acta Crystallogr. B* **1973**, *29*, 2046−2056.

(28) Hohenberg, P.; Kohn, W. Inhomogeneous Electron Gas. *Phys. Rev.* **1964**, *136*, B864−B871.

(29) Kohn, W.; Sham, L. J. Self-consistent Equations Including Exchange and Correlation Effects. *Phys. Rev.* **1965**, *140*, A1133−A1138.

(30) Perdew, J. P.; Burke, K.; Ernzerhof, M. Generalized Gradient Approximation Made Simple. *Phys. Rev. Lett.* **1996**, *77*, 3865−3868.

(31) Kresse, G.; Hafner, J. Ab initio Molecular Dynamics for Open-Shell Transition Metals. *Phys. Rev. B* **1993**, *48*, 13115−13118.

(32) Kresse, G.; Furthmüller, J. Efficient Iterative Schemes For Ab Initio Total-Energy Calculations Using a Plane-Wave Basis Set. *Phys. Rev. B* **1996**, *54*, 11169−11186.

(33) Blöchl, P. E. Projector Augmented-Wave Method. *Phys. Rev. B* **1994**, *50*, 17953−17979.

(34) Kresse, G.; Joubert, D. From Ultrasoft Pseudopotentials to the Projector Augmented-Wave Method. *Phys. Rev. B* **1999**, *59*, 1758−1775.

(35) Monkhorst, H. J.; Pack, J. D. Special Points for Brillouin-Zone Integrations. *Phys. Rev. B* **1976**, *13*, 5188−5192.

(36) Dickens, B.; Bowen, J. S. Refinement of the Crystal Structure of $Ca(H_2PO_4)_2{\cdot}H_2O$. *Acta Crystallogr. B* **1971**, *27*, 2247−2255.

(37) Hughes, J. M.; Cameron, M.; Crowley, K. D. Structural Variations in Natural F, OH, and Cl Apatites. *Am. Mineral.* **1989**, *74*, 870−876.

(38) Chiatti, F.; Corno, M.; Ugliengo, P. Stability of the Dipolar (001) Surface of Hydroxyapatite. *J. Phys. Chem. C* **2012**, *116*, 6108−6114.

(39) Bittencourt, A. F. B.; Mendes, P. C. D.; Valença, G. P.; Da Silva, J. L. F. Acid-Base Properties of Hydroxyapatite(0001) by the Adsorption of Probe Molecules: An Ab Initio Investigation. *Phys. Rev. Mater.* **2021**, *5*, No. 075003.

(40) Elliott, J. C. *Structure and Chemistry of the Apatites and Other Calcium Orthophosphates*; Elsevier: Amsterdam, Netherlands, 1994.

(41) None Available Materials Data on $CaP_2(HO_2)_4$ by Materials Project 2020 https://www.osti.gov/servlets/purl/1200054/.

(42) Jain, A.; Ong, S. P.; Hautier, G.; Chen, W.; Richards, W. D.; Dacek, S.; Cholia, S.; Gunter, D.; Skinner, D.; Ceder, G.; Persson, K. A. Commentary: The Materials Project: A Materials Genome Approach to Accelerating Materials Innovation. *APL Mater.* **2013**, *1*, No. 011002.

(43) Pearson, R. G. Chemical Hardness and Density Functional Theory. *J. Chem. Sci.* **2005**, *117*, 369−377.

(44) Schira, R.; Latouche, C. DFT and Hybrid-DFT Calculations on the Electronic Properties of Vanadate Materials: Theory Meets Experiments. *New J. Chem.* **2020**, *44*, 11602−11607.

(45) Su, X.; Chu, Y.; Yang, Z.; Lei, B.-H.; Cao, C.; Wang, Y.; Liu, Q.; Pan, S. Intense d-p Hybridization Induced a Vast SHG Response Disparity Between Tetrahedral Vanadates and Arsenates. *J. Phys. Chem. C* **2020**, *124*, 24949−24956.

(46) Guerra-López, J. R.; Bianchi, A. E.; Ramos, M. A.; Ferraresi-Curotto, V.; Güida, J. A.; Echeverría, G. A. Novel Synthesis and Crystallographic Results of Zinc Substituted Hydroxyapatite with High Thermal Stability. *Phys. B* **2024**, *676*, No. 415676.

(47) Terra, J.; Gonzalez, G. B.; Rossi, A. M.; Eon, J. G.; Ellis, D. E. Theoretical and Experimental Studies of Substitution of Cadmium into Hydroxyapatite. *Phys. Chem. Chem. Phys.* **2010**, *12*, No. 15490.

(48) Terra, J.; Dourado, E. R.; Eon, J.-G.; Ellis, D. E.; Gonzalez, G.; Rossi, A. M. The Structure of Strontium-Doped Hydroxyapatite: An Experimental and Theoretical Study. *Phys. Chem. Chem. Phys.* **2009**, *11*, 568−577.

(49) Landi, E.; Logroscino, G.; Proietti, L.; Tampieri, A.; Sandri, M.; Sprio, S. Biomimetic Mg-Substituted Hydroxyapatite: From Synthesis to in Vivo Behaviour. *J. Mater. Sci.:Mater. Med.* **2008**, *19*, 239−247.

(50) Shi, H. B.; Tian, X.; Zhong, H.; Liu, Y.; Wan, T. Preparation of Strontium-Barium Hydroxyapatite by Coprecipitation. *Adv. Mater. Res.* **2013**, *690−693*, 1524−1528.